CD20 targeted nanomedicine for GCB-diffuse large B-cell lymphoma through synergistic effects of apoptosis and ferroptosis

Shu-xian Liu [a,1], Jun-yu Zhang [b,1], Xiao-yan Zheng [c,1], Yong-zhong Du [d,*], Xiang-min Tong [e,**]

[a] *Key Laboratory of Elemene Class Anti-Cancer Chinese Medicines, School of Pharmacy, Hangzhou Normal University, Hangzhou, Zhejiang, 311121, China*
[b] *The Fifth Affiliated Hospital of Wenzhou Medical University, Lishui Central Hospital, Lishui Hospital of Zhejiang University, Lishui, 323000, Zhejiang Province, China*
[c] *The Quzhou Affiliated Hospital of Wenzhou Medical University, Quzhou People's Hospital, Quzhou, Zhejiang, 324000, China*
[d] *Institute of Pharmaceutics College of Pharmaceutical Sciences, Zhejiang University, 866 Yu-Hang-Tang Road, Hangzhou, 310058, China*
[e] *Department of Hematology, The Affiliated Hangzhou First People's Hospital, Westlake University School of Medicine, Hangzhou, 310006, China*

ARTICLE INFO

ABSTRACT

Diffuse large B-cell lymphoma (DLBCL) is one of the most prevalent lymphomas, and can be classified as activated B-cell DLBCL (ABC-DLBCL) or germinal center B-cell DLBCL (GCB-DLBCL) according to molecular subtypes. Studies have shown that drug resistance is an important factor in its therapeutic failure. Tumor-specific drug delivery nanocarriers may be a promising strategy for the treatment of lymphoma. Herein, we developed a nanomedicine (RTX-DOX/DMF-Lip, RDDL) carrying the chemotherapeutic drugs doxorubicin (DOX) and dimethyl fumarate (DMF), and surface-modified with rituximab (RTX), which can recognize CD20 antigen when it comes into contact with the surface of a B-lymphoma cell. In the study, we found that DOX and DMF can be delivered to the tumor site precisely and demonstrate a potent synergistic anti-tumor effect. Once the nanomedicine was internalized, it induced apoptosis through ROS generation and the activation of caspase-3. Concurrently, DMF directly reduced the levels of glutathione (GSH) in tumor cells by inhibiting System Xc⁻, thereby resulting in impaired ROS detoxification and fostering an environment conducive to lipid peroxidation (LPO) and ferroptosis. Furthermore, the ROS generated by DOX synergistically propelled the process of ferroptosis, creating a potent therapeutic effect. These effects were validated in the GCB-DLBCL mouse model, where RDDL had a more potent killing effect compared to free drugs by striking SU-DHL-10 cells through a dual mechanism of apoptosis and ferroptosis, providing a new therapeutic strategy for the treatment of drug-resistant GCB-DLBCL.

1. Introduction

Diffuse large B-cell lymphoma (DLBCL) is the most common type of non-Hodgkin's lymphoma (NHL), accounting for about 30–40% of all NHL cases [1–3]. DLBCL exhibits significant molecular heterogeneity and complex biological characteristics. Based on immunohistochemical (IHC) classification, it can be divided into germinal center B-cell-like (GCB)-DLBCL and activated B-cell like (ABC)-DLBCL and a few indistinguishable tertiary types [2,4–7]. Currently, the standard first-line chemotherapy for DLBCL is the R-CHOP regimen, which combines rituximab (RTX) with cyclophosphamide, doxorubicin (DOX), vincristine, and prednisone, and achieves remission in approximately 70% of patients. Nevertheless, 30–40% of patients still face a poor prognosis [8,9].

It is widely recognized that the anthracycline drug DOX represents therapeutic effects in a diverse range of cancers, including breast cancer, gastric cancer, lymphoma and others [10]. Evidently, DOX plays a crucial role in R-CHOP and induces apoptosis in DLBCL cells [11,12]. Apoptosis is a normal physiological cell death response to diverse stimuli, infections, or injuries, which has a vital function in the maintenance of cellular homeostasis and is executed through a diverse array of action mechanisms [13,14]. DOX triggers apoptosis *via* two primary mechanisms: the first involves intercalating into the double-stranded DNA molecule by forming hydrogen bonds with guanine, resulting in a positive supercoiling of DNA, which prevents the DNA from completing replication properly [15,16]; another way is that DOX binds to cardiolipin located on the inner mitochondrial membrane, causing a

rise in intracellular reactive oxygen species (ROS) [17]. Excessive ROS disrupts the mitochondrial structure and induces intracellular oxidative stress, as well as up-regulating the expression of Bax protein, caspase 3, and down-regulating of bcl-2 expression, leading to the death of cancer cells [18–21].

While most conventional cancer therapies, including chemotherapy and radiation, primarily target apoptosis pathways to eliminate malignant cells, tumor cells often develop resistance mechanisms to evade apoptosis, resulting in reduced cancer efficacy as well as increased recurrence rates [22,23]. Among these, the glutathione (GSH)-mediated antioxidant defense system plays a pivotal role in protecting tumor cells from oxidative stress. GSH, a non-enzymatic antioxidant, typically exists in its reduced form. It can react with ROS to generate oxidized glutathione (GSSG), which can be used by tumor cells to alleviate the intracellular oxidative stress state and thus maintain the intracellular redox balance [24,25]. Studies have revealed that overexpression of GSH in tumor cells substantially attenuates DOX-induced apoptosis. Conversely, the depletion of GSH results in the accumulation of intracellular ROS and irreversible oxidative damage [26]. These findings collectively suggest that targeted depletion of intracellular GSH could serve as an effective therapeutic approach to amplify ROS-mediated apoptosis and overcome chemoresistance in cancer treatment.

Ferroptosis is a novel iron-dependent mode of cell death that is mechanistically and morphologically distinct from apoptosis, autophagy, and pyroptosis, and can be initiated by both exogenous and endogenous pathways [27,28]. Cystine-glutamate antiporter system (System Xc$^-$) plays a central role in ferroptosis [29]. Inhibition of System Xc$^-$ impairs cystine uptake, resulting in GSH depletion and consequent inactivation of glutathione peroxidase 4 (GPX4). This inactivation triggers a rapid accumulation of phospholipid hydroperoxides (PLOOHs), which disrupts the plasma membrane and leads to cell death [30].

Dimethyl fumarate (DMF) is currently the first-line drug for the treatment of relapsing-remitting multiple sclerosis (RRMS), and has gradually gained attention in anti-tumor in recent years. Existing research has revealed that DMF can specifically induce ferroptosis in GCB-DLBCL cells by reducing intracellular GSH through inhibition of System Xc$^-$ [31,32]. It is worthy of note that, despite the fact that the depletion of GSH diminishes the antioxidant capacity of tumor cells, the production of ROS and lipid peroxidation (LPO) is frequently constrained [33,34]. Interestingly, DOX not only induces DNA damage in tumor cells, but also promotes the generation of ROS by upregulating nicotinamide adenine dinucleotide phosphate oxidase 4 (NOX4) [35, 36].

Consequently, the combination of DOX and DMF is expected to induce ferroptosis and exacerbate DOX-mediated oxidative stress *via* GSH depletion. Concurrently, DOX potentiates DMF-induced ferroptosis, creating a positive feedback loop. This combinatorial strategy significantly enhances tumor cell sensitivity to both apoptosis and ferroptosis, thereby overcoming resistance to conventional apoptosis therapies. Nevertheless, the traditional method of simply and directly combining the two drugs is far from ideal. Differences in pharmacokinetics, physicochemical properties and biodistribution of different drugs often lead to suboptimal chemotherapeutic effects with systemic administration [37]. Additionally, DOX is known to have serious toxic side effects, such as alopecia, vomiting and cardiotoxicity, which greatly limits its clinical application [38,39].

As previously discussed, in our study, we successfully developed a CD20-targeted nanosystem by co-encapsulating DOX and DMF within RTX-functionalized liposomes (RTX-DOX/DMF-Lip, RDDL), which has the ability to target the GCB-DLBCL surface-specific antigen CD20, with a favorable biosafety profile. Our findings revealed that DOX and DMF exhibit a potent synergistic anti-tumor effects, and the prepared nanosystem enables synchronous spatiotemporal delivery of the two drugs. DMF induces ferroptosis and enhances the oxidative stress response of DOX by decreasing GSH in SU-DHL-10 cells (GCB-like). Meanwhile, the ROS accumulation induced by DOX positively contributes to DMF-

induced ferroptosis. Furthermore, this nanosystem lead to alterations in the expression levels of caspase 3, bcl-2 family proteins and GPX4 in SU-DHL-10 cells. *In vivo* studies demonstrated the RDDL has excellent tumor-targeting capability, with preferential accumulation in tumor tissues, leading to significant growth inhibition. In conclusion, our work has demonstrated for the first time the synergistic anti-tumor effects of DOX and DMF, the RDDL achieves potent cooperative therapeutic effects through dual mechanisms of apoptosis and ferroptosis, representing an effective targeted delivery strategy for the treatment of GCB-DLBCL.

2. Materials and methods

2.1. Preparation materials

Egg yolk lecithin and cholesterol (Chol) were purchased from Yien Chemical Technology Co., Ltd. (Shanghai, China). Dimethyl fumarate (DMF) was obtained from MedChemExpress (MCE). Rituximab (RTX) injection was from Roche Pharmaceutical Co., Ltd. (Shanghai, China). 1,2-distearoyl-sn-glycero-3-phosphoethanolamine-N-[maleimide(polyethyleneglycol)] (DSPE-PEG-MAL) was purchased from Tuoyang Biotechnology Co., Ltd. (Shanghai, China). Traut's reagent, glutathione (GSH) and vitamin E (VE) were purchased from Aladdin Bio-Chem Technology Co., Ltd (Shanghai, China). Ferrostatin-1 (Fer-1) was purchased from Sigma-Aldrich (St. Louis, MO, USA). DFO was obtained from Shanghai Yuanye Bio-Technology Co., Ltd. (Shanghai, China). Doxorubicin hydrochloride (DOX), RPMI-1640, DMEM, fetal bovine serum (FBS), penicillin-streptomycin solution and trypsin were obtained from Dalian Meilun Biotech Co., Ltd. The CCK-8 kit, hypersensitive ECL chemiluminescence kit, BCA protein concentration determination kit, caspase 3 activity assay kit, 4′,6′-diamidino-2-phenylindole (DAPI), Annexin V-FITC/PI apoptosis detection kit, Calcein/PI live/dead viability/cytotoxicity kit, 2,7-dichlorofluorescein diacetate (DCFH-DA), GSH assay kit, lipid peroxidation MDA assay kit, mitochondrial membrane potential assay kit with JC-1, matrix-gel basement membrane matrix were purchased from Beyotime Biotechnology Co., Ltd. (Shanghai, China). Anti-bcl-2 rabbit mAb, anti-Bax rabbit mAb, [KO Validated] anti-p53 rabbit mAb, anti-CD20 rabbit mAb, ABflo® 647 rabbit anti-human/monkey CD20 mAb were obtained from ABclonal Biotech Co., Ltd. (Wuhan, China). β-actin monoclonal antibody was from Proteintech Group Inc. (Wuhan, China). Anti-glutathione peroxidase 4 (GPX4) rabbit mAb was purchased from Bioswamp Biotech Co., Ltd. (Wuhan, China). β-tubulin rabbit mAb was obtained from Signalway Antibody LLC. (USA). The BODIPY581/591-C11 probe was from Thermo Fisher Scientific (Waltham, MA, US). HRP goat anti-mouse IgG (H + L) antibody and HRP goat anti-rabbit IgG (H + L) antibody were purchased from APE × BIO Technology LLC. (USA).

2.2. Synthesize of the RTX-PEG-DSPE

RTX was conjugated to DSPE-PEG-MAL using a previously reported method. Briefly, RTX:2-IT = 1:20 (mol/mol) was incubated at 37°C for 2 h to obtain thiolated RTX (SH-RTX). Then, used an ultrafiltration tube with a molecular weight cutoff (MWCO) of 10 kDa to remove excess 2-IT by centrifugation at 2500 rpm for 10 min. DSPE-PEG-MAL (10 mg) was dissolved in purified water, added to SH-RTX (4 mg), and then incubated at 4 °C overnight to obtain RTX-PEG-DSPE. The mixture was dialysis against PBS using a cellulose ester dialysis membrane and stored at 4°C. RTX-PEG-DSPE was characterized by the Fourier transform infrared (FT-IR) spectroscopy (IFS 55, Bruker, Germany) and ^{1}H nuclear magnetic resonance (NMR) analysis (500 MHz, Bruker, Switzerland). The protein coupling rate was measured by BCA protein concentration determination kit.

2.3. Preparation and characterization of RDDL

RDDL were prepared using the thin-film dispersion and ammonium sulfate gradient method as follows: In a round bottom flask, a mixture of lecithin and Chol at a mass ratio (3:1) was completely dissolved in chloroform containing DMF. Subsequently, a rotary evaporator was employed to form a lipid thin film. The dried film was hydrated with 155 mmol/L $(NH_4)_2SO_4$ solution, vortexed for 5 min and subjected to probe ultrasound for 10 min to facilitate liposomes. Then, the liposomes were dialyzed overnight against normal PBS in dialysis bags (Beijing Solarbio Science&Technology Co.,Ltd) with MWCO of 8000–14000 to remove $(NH_4)_2SO_4$ solution in the external aqueous phase. Finally, RTX-DSPE-PEG and DOX were added to the dialyzed liposomes and placed in a constant temperature water bath at 40°C for 2 h, and then stored in a 4°C refrigerator.

The morphology, size distribution, zeta potential and drug loading capacity of RDDL were characterized. Transmission electron microscopy (TEM; JEM-1400flash, JEOL, Japan) was used to investigate morphology of RDDL. Size distribution and zeta potential data were measured *via* dynamic light scattering (DLS; Litesizer 500, Anton-Paar, Austria). Absorbance of DOX and DMF was determined by UV–vis spectrophotometer (UV-2600, SHIMADZU, Japan). The drug loading capacity of DOX was determined by UV–vis spectrophotometry, whereas DMF was determined by high performance liquid chromatography (HPLC). The drug loading amount was calculated by the following formula: Drug loading (wt.%) = (mass of drug in nano drug/total mass of nano drug) × 100 %.

2.4. In vitro release test

Dialysis was applied to evaluate the cumulative release profiles of DOX and DMF from liposomes. Dialysis bags (MWCO 8000–14,000) were loaded with 2 mL of DOX, DMF, RDDL, respectively. The bags were immersed in 8 mL of PBS (pH = 7.4) and stirred at 60 rpm under 37 °C. The cumulative drug release percentages of DOX and DMF were determined using pre-established standard curves.

2.5. Cell culture

SU-DHL-10, MCF-7, Jurkat and K562 cells were used in this study. SU-DHL-10, Jurkat and K562 cells were cultured in complete RPMI-1640 cell culture medium with 10% FBS and 1% penicillin-streptomycin. MCF-7 cells were in DMEM cell culture medium with 10% FBS and 1% penicillin−streptomycin. All cell cultures were maintained in a 37°C incubator with 5% CO_2.

2.6. In vitro cell viability test and combination index calculation

SU-DHL-10 cells in the logarithmic growth phase were seeded into a 96-well plate at a density of $1–5 \times 10^4$ cells per well in 90 μL culture media, each group was established in triplicate. 10 μL different formulations (PBS, DMF, DOX, DOX + DMF, DDL, RDDL) were added, with a final DOX concentration gradient of 1 μg/mL. The plates were then incubated in a 37 °C, 5 % CO_2 incubator. After being incubated for 24 h, add 10 μL CCK-8 reagent to each well and incubating for an additional 4–5 h. The absorbance at 450 nm was measured by a microplate reader. Cell viability was calculated according to the following formula: Cell viability (%) = (A$_{sample}$-A$_{blank}$)/(A$_{control}$-A$_{blank}$) × 100 %.

To determine the optimal concentrations for combination treatment, a range of drug concentrations was established. Specifically, concentration gradients of DOX (0, 0.5, 1, 1.5, 2, 2.5 μg/mL) and DMF (0, 10, 15, 20, 25, 30, 35, 40 μg/mL) were employed. Combination index (CI) was calculated with the CompuSyn software. The interpretation criteria were as follows: CI > 1, indicating mutual antagonism; CI = 1, indicating superposition; CI < 1, indicating synergy.

2.7. In vitro cellular uptake of RDDL

SU-DHL-10 cells in the logarithmic growth phase were seeded into 12-well plates at a density of $1–5 \times 10^5$ cells/well, and treated with DOX, DDL and RDDL (with final concentrations equivalent to 1 μg/mL DOX) and incubated for 1, 2, 4, and 8 h. Upon reaching the time point, cells were collected by centrifugation, washed twice with PBS, and fixed with 4 % paraformaldehyde (PFA) for 30 min. Then stain them with DAPI for 15 min avoiding light. After staining, cells were washed and suspended with PBS. 10 μL of cell suspension was dropped on a slide-proof slide (1 % poly-L-lysine hydrobromide treated). Fluorescence imaging was performed using a confocal laser scanning microscope (CLSM; A1R, Nikon, Japan) with a 488 nm laser excitation source to visualize DOX fluorescence.

Similarly, SU-DHL-10 cells were seeded into 24-well plates at a density of $1–5 \times 10^5$ cells/well, treated with DOX, DDL and RDDL (with final concentrations equivalent to 1 μg/mL DOX) and incubated for 1, 2, 4, and 8 h. The cells were harvested and resuspended in 200 μL PBS. Flow cytometry (FCM) analysis was performed using Flow cytometry (FCM; ACEA NovoCyteTM, ACEA Biosciences, USA). The FITC signal channel was selected to detect the fluorescence of DOX.

2.8. Detection of live/dead cells

SU-DHL-10 cells in the logarithmic growth phase were seeded into 6-well plates at a density of $1–5 \times 10^5$ cells/well, treated with PBS, DMF, DOX, DOX + DMF, DDL and RDDL (with final concentrations equivalent to 1 μg/mL DOX) and incubated for 24 h. Subsequently, the cells were treated with calcein acetoxymethyl ester (Calcein AM) and propidium iodide (PI) for 30 min. Ultimately, the cells underwent multiple rinses with PBS and were visualized using the inverted fluorescence microscope.

2.9. Detection of apoptosis

SU-DHL-10 cells in logarithmic growth phase were seeded into 12-well plates at a density of 5×10^5 cells/well, treated with PBS, DMF, DOX, DOX + DMF, DDL and RDDL (with final concentrations equivalent to 1 μg/mL DOX). After incubating for 24 h, cells were collected and centrifuged at 1000 rpm for 5 min, resuspended in 195 μL of Annexin V binding buffer. Then, 5 μL of Annexin V-FITC and 10 μL of PI staining solution were added sequentially, gently vortexed and incubated at 37°C in the dark for 10–20 min. Finally, placed cells in an ice bath for FCM analysis.

2.10. Detection of MMP

Mitochondrial membrane potential (MMP) changes were detected using the JC-1 assay kit. Under normal conditions, JC-1 exists as aggregates emitting red fluorescence (590 nm), whereas when the MMP is depolarized, JC-1 monomers emit green fluorescence (525 nm). SU-DHL-10 cells in logarithmic growth phase were seeded into 12-well plates at a density of 5×10^5 cells/well, treated with PBS, DMF, DOX, DOX + DMF, DDL and RDDL (with final concentrations equivalent to 1 μg/mL DOX) for 24 h. Cells were then collected and stained with JC-1 assay working solution for 30 min at 37°C in the dark. Fluorescence intensity was immediately analyzed by FCM.

2.11. Detection of caspase 3 activity

Changes in Caspase 3 activity in cells were detected using the caspase 3 activity assay kit, which measures the caspase 3-catalyzed production of yellow-colored p-nitroanilides (pNAs). SU-DHL-10 cells in logarithmic growth phase were seeded into 12-well plates at a density of 5×10^5 cells/well, treated with PBS, DMF, DOX, DOX + DMF, DDL and RDDL (with final concentrations equivalent to 1 μg/mL DOX). After incubating

for 24 h, cells were harvested by centrifugation at 1000 rpm for 5 min. The cell pellets were resuspended in RIPA lysis buffer and lysed on ice for 15 min, then centrifuged at 20,000 g for 10 min. The supernatant was incubated with the assay solution for 1 h at 37 °C. Finally, the absorbance was measured at 405 nm using a microplate reader.

2.12. Detection of ROS level

ROS generation was detected by DCFH-DA probe. SU-DHL-10 cells in logarithmic growth phase were seeded into 12-well plates at a density of 5×10^5 cells/well. After stimulating the cells with PBS, DMF, DOX, DOX + DMF, DDL and RDDL (with final concentrations equivalent to 1 μg/mL DOX) for 12 h, the cells were collected. Cells were washed twice with PBS and resuspended in 500 μL of DCFH-DA probe (1:8000 dilution), then incubated at 37°C for 15 min in the dark. Finally, the intensity of DCF fluorescence was immediately observed by CLSM and analyzed quantitatively by FCM.

2.13. In vitro GSH assessment

SU-DHL-10 cells in logarithmic growth phase were seeded into 12-well plates at a density of 5×10^5 cells/well, treated with PBS, DMF, DOX, DOX + DMF, DDL and RDDL (with final concentrations equivalent to 1 μg/mL DOX). Following the instructions of the GSH assay kit, the harvested cells were repeatedly frozen-thawing for 3 times in liquid nitrogen at 37 °C. Subsequently, the cell lysates were centrifuged at 10,000 g for 10 min to collect the supernatant. Next, mix with 10 μL DTNB. The absorbance was measured at 412 nm after incubation for 30 min. In addition, the supernatant protein concentration was determined using the BCA protein assay kit to normalize the GSH content.

2.14. In vitro LPO assessment

In order to monitor the induction of ferroptosis, the BODIPY 581/591C11 probe was employed to detect LPO. In brief, SU-DHL-10 cells in logarithmic growth phase were seeded into 12-well plates at a density of 5×10^5 cells/well, the cells were incubated with PBS, DMF, DOX, DOX + DMF, DDL and RDDL (with final concentrations equivalent to 1 μg/mL DOX) for 24 h. Then, cells were stained with 2 μM of BODIPY 581/591C11 for 15 min at 37°C. After washing, cells were immediately observed by CLSM and analyzed quantitatively by FCM.

MDA assay kit was used to measure aldehydes produced by LPO of unsaturated fatty acids. SU-DHL-10 cells were treated as previously described. Cells were harvested by centrifugation at 1000 rpm for 5 min. After lysing the cells on ice with 100 μL of lysate, the supernatant was centrifuged, mixed with thiobarbituric acid (TBA) reagent, boiled at 100 °C for 15 min, cooled to room temperature, then measured the absorbance of the supernatant at 523 nm. At the same time, the protein concentration of each supernatant was quantified with a BCA protein assay kit to normalize the MDA content.

2.15. Western blotting analysis

SU-DHL-10 cells were seeded in 12-well plates at a density of 5×10^5 cells/well, then subjected to the same treatment as described above. After co-incubation with cells for 24 h, cells were collected and centrifuged at 1000 rpm for 5 min, discarded the supernatant and added RIPA lysis solution (contained PMSF and protease inhibitors), ice bath for 10–15 min. Then cell lysates were centrifuged at 12,000 g for 10 min at 4 °C. Protein content was normalized using the BCA kit. Subsequently, proteins were separated by 4–12 % SDS-PAGE, using the antibody and secondary antibody of the corresponding species, and developed by ECL luminescent solution.

2.16. Animal models

Female BALB/c-nude mice (16–20 g) were obtained from the Shanghai Silaike Laboratory Animal Limited Liability Company. All mice were pathogen-free and fed enough food and water. SU-DHL-10 cells in the logarithmic growth phase were adjusted to a concentration of 1×10^7 cells/mL, mixed 1:1 with matrigel. Subcutaneously injected 0.1 mL the cell-matrigel mixture into the right forearm of each mouse. When the average tumor volume reached approximately 100 ± 10 mm³, the following experiments could be conducted.

2.17. In vivo biodistribution

The distribution of the nanosystem was detected by an *in vivo* imaging system (IVIS Spectrum, Caliper, USA). The mice were given 0.1 mL DiD-Lip, RTX-DiD-Lip (concentration of DiD was 0.04 mg/mL) *via* tail vein injection when the tumors reached a volume about 200 ± 10 mm³. The mice were imaged at 3, 6, 9, 12 and 24 h postinjection. Additionally, mice were sacrificed to investigate the distribution of fluorescence in major organs and tumor tissues.

2.18. In vivo anti-tumor therapy

Once tumor volume reached 100 ± 10 mm³, the tumor-bearing mice were randomized into six groups: (1) PBS; (2) DMF; (3) DOX; (4) DOX + DMF; (5) DDL; and (6) RDDL (n = 5). The tumor-bearing mice were then treated with different formulations at a frequency of every two days for a total of three times. DMF was administered *via* intraperitoneal injection at 50 mg/kg, while other groups *via* the tail vein at equivalent DOX (5 mg/kg). The tumor volume of mice were regularly measured every 2 days, and was calculated using the formula: tumor volume (V) = (length × width²)/2. After sacrifice, tumors were harvested, formalin-fixed, embedded in paraffin, and sectioned. Sections were stained with H&E and TUNEL staining. Afterwards, the protein expression of caspase 3, p53, Bax, bcl-2 and GPX4 was evaluated by immunohistochemistry.

2.19. In vivo biosafety evaluation

To investigate the biosafety of RDDL, orbital blood was collected from mice for hemolysis experiments. Subsequently, the erythrocytes were separated by centrifugation at 3000 rpm for 5 min and diluted with PBS in triplicate. The Triton X-100, PBS, and RDDL solutions were then incubated with the erythrocytes for 1 h at 37°C to observe and compare the hemolysis results.

To assess the toxicity of each group of preparations, we recorded the weight of mice every two days. The mice were sacrificed on day 21, and the heart, liver, spleen, lung, kidney and blood samples were collected from tumor-bearing mice. Major organs were fixed with 4% PFA and used for H&E staining, and blood samples were used for blood biochemical analysis.

2.20. Statistical analysis

Statistical analysis was conducted by utilizing Graphpad Prism 9.5.0 software. All results were presented as the Mean ± SEM. Student's t-test was used for comparison of two groups and one-way ANOVA for multiple groups. *P < 0.05, **P < 0.01, ***P < 0.001, and ****P < 0.0001.

3. Results and discussion

3.1. Synergistic effect of DOX and DMF

Before synthesizing the liposomes, the effects of DOX and DMF on SU-DHL-10 cells were first investigated. The half maximal inhibitory concentration (IC50) value of DOX and DMF were 1 μg/mL and 11 μg/mL, respectively (Fig. S1). To determine the optimal drug concentrations

for maximal cytotoxic effects, we then performed dose-response experiments by incubating SU-DHL-10 cells with varying concentrations of DOX and DMF. The CI values were calculated based on the results of a concentration gradient assay. We were surprised to find that when the DOX concentration was 1 µg/mL, the CI values of the DMF concentration range from 5 to 20 µg/mL were all lower than 1, indicating that the cytotoxicity was promoted in all this range (Fig. 2A, Fig. S2). Consequently, we selected a DOX concentration of 1 µg/mL and a DMF concentration of 10 µg/mL for further studies, and the CI value was 0.8204 at this specific concentration combination.

3.2. Preparation and characterization of RDDL

DOX/DMF-Lip (DDL) and RTX-DOX/DMF-Lip (RDDL) were prepared following the methods described in the experimental section. The water-soluble drug DOX, and the fat-soluble drug DMF were encapsulated in our synthesized liposomes, then the RTX underwent thiolated and was subsequently conjugated *via* the maleimide (MAL) group (Fig. 1, Fig. S3).

The ^{1}H NMR spectrum successfully verified the connection between RTX and DSPE-PEG-MAL [40–42]. When D_2O was employed as the solvent, the characteristic peak attributed to the -CH=CH- group in the MAL was located at 6.8 ppm. Notably, in the spectrum of RTX-PEG-DSPE, the peak at 6.8 ppm has vanished (Fig. S4). FT-IR spectroscopy was also employed to verify the functionalization of the conjugates (Fig. S5). In the RTX spectrum, the N-H stretching vibration (3300 cm^{-1}), the N-H bending vibration (1550 cm^{-1}) and the C=O stretching vibration (1650 cm^{-1}) can be seen, which are the characteristic peaks of amide bonds. In the FT-IR spectrum of RTX-PEG-DSPE, the characteristic peaks of amide bonding can also be observed. Moreover, the characteristic peaks of polyethylene glycol (PEG) can be found

in its spectrum: the C-H stretching vibrations at 2920 cm^{-1} and 2870 cm^{-1}, and the C-O stretching vibration at 1100 cm^{-1}. These are consistent with those shown in the DSPE-PEG-MAL. The above results provided convincing evidence for the linkage of sulfhydryl groups to MAL. The successful conjugation of RTX to liposomes was thoroughly characterized by means of SDS-PAGE. As shown in Fig. S6, the 147 kDa RTX showed a slight shift upon conjugation with the liposome. And the coupling efficiency was determined to be 74.10 ± 5.36 % through the BCA assay.

DLS analysis revealed that, with the drug loaded, the hydration sizes of blank-L (102.16 nm), DDL (132.13 nm) and RDDL (138.01 nm) increased in sequence (Fig. 2B). Meanwhile, polydispersity index (PDI) of blank-L, DDL, and RDDL was 0.191, 0.244 and 0.240, respectively (Fig. S7A–C). Zeta potential was −7.4 mV, −7.95 mV, and −9.61 mV, respectively (Fig. S7D). The characterization of liposome was also observed by the TEM, which visualized a phospholipid bilayer spherical structure with a particle size uniform to the hydrated particle size, further confirming the successful synthesis of liposomes (Fig. 2C). Meanwhile, the stability of RDDL was assessed by storing at 4°C for one week. The particle size remained within 150 nm, and the PDI was maintained at approximately 0.2 (Fig. 2D), indicating excellent stability of the RTX-modified liposomes and suggesting suitability for further *in vitro* and *in vivo* studies. The UV–vis spectrum identified the maximum absorption wavelengths for DOX and DMF as 480 nm and 214 nm, respectively, which were utilized for drug concentration determination (Fig. 2E). The encapsulated efficiency (EE) and drug loading (DL) capacity of DOX were 94.63 ± 0.78% and 6.60 ± 5.34%, respectively; the values of DMF were 98.54 ± 1.32% and 4.69 ± 0.63%, respectively. The *in vitro* release studies of free DOX and DMF, as well as DOX and DMF from RDDL in PBS (pH = 7.4) were also investigated. As shown in Fig. 2F, While 87% of free DOX and 91% of free DMF were released
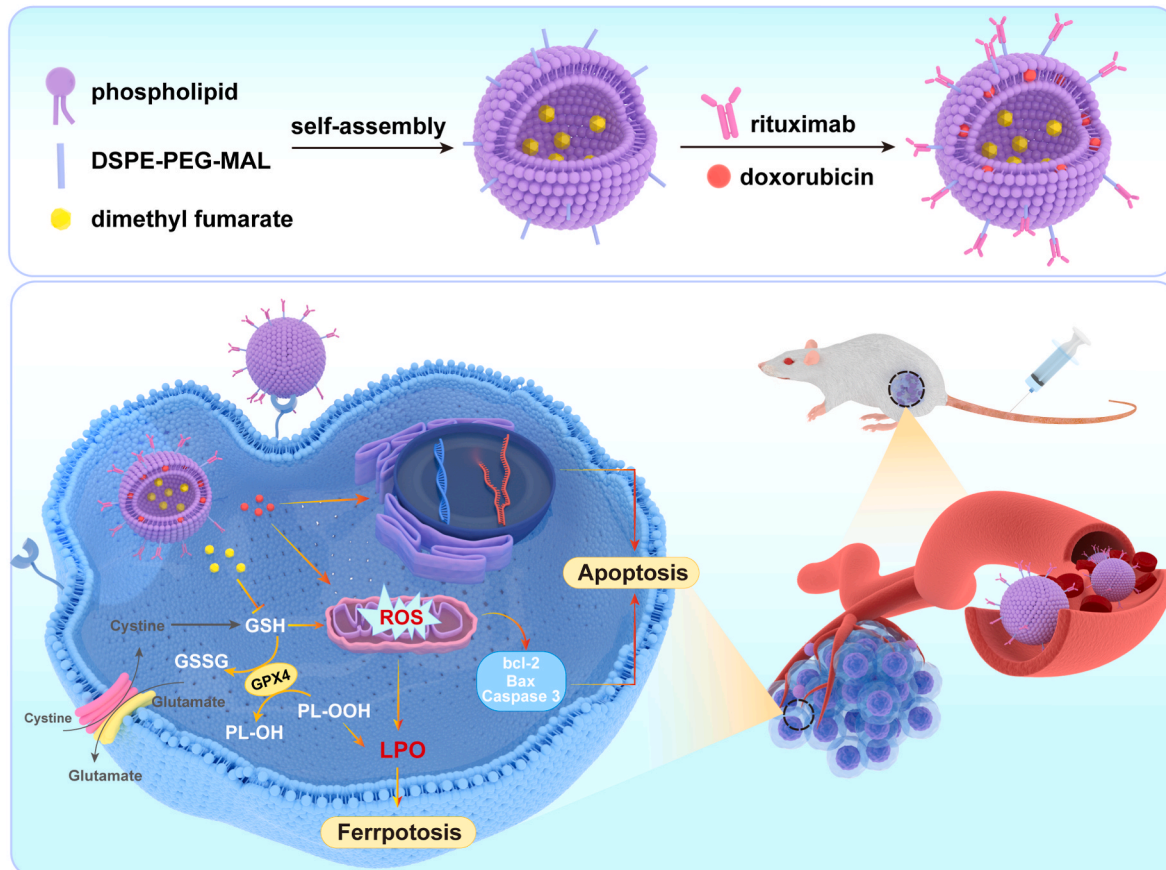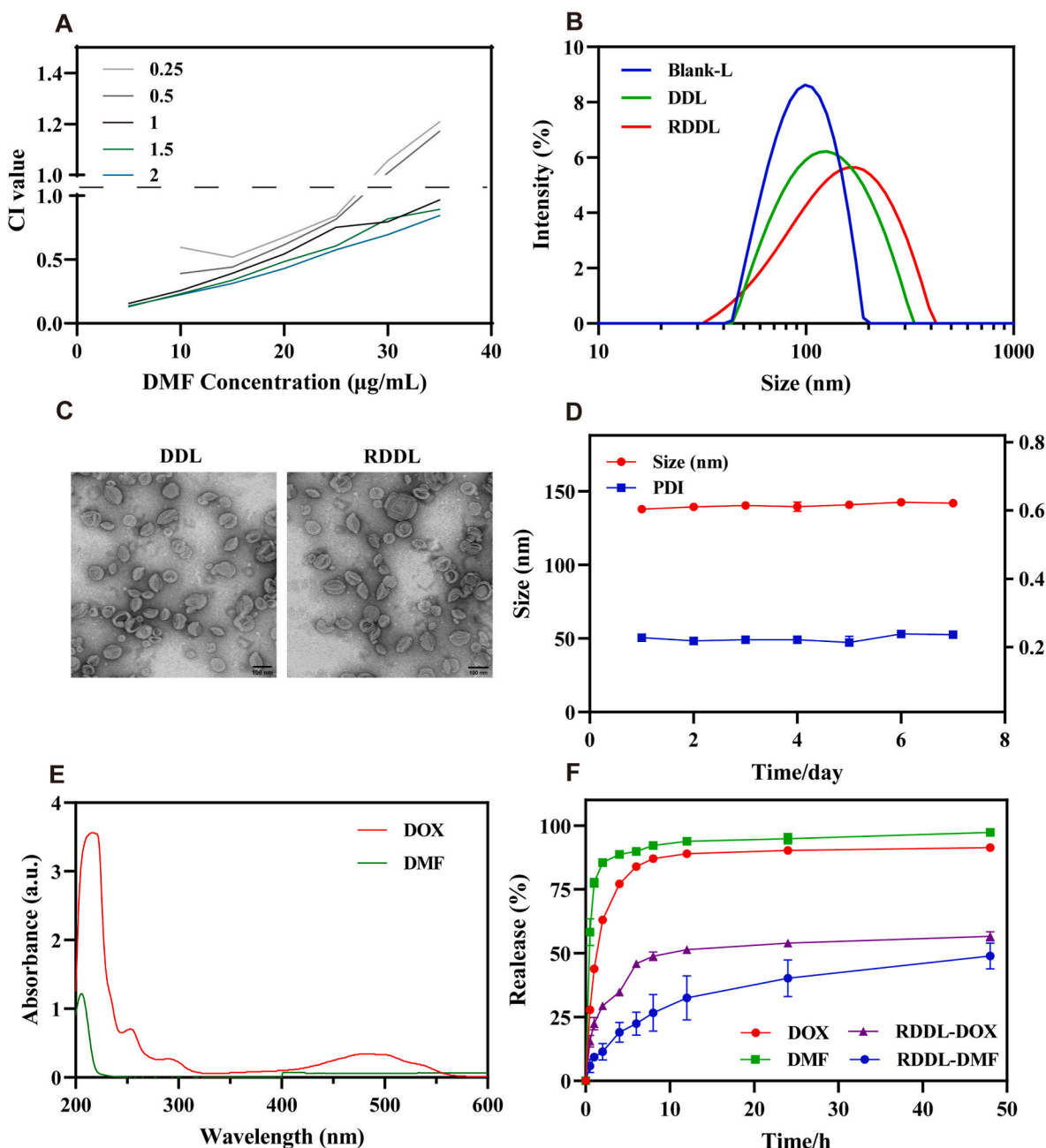

Fig. 1. Schematic illustration of the preparation process and anti-tumor process of RDDL by inducing enhanced apoptosis and ferroptosis.

Fig. 2. Characterization of RDDL. (A) The combination index (CI) of DOX and DMF in different ratio against SU-DHL-10 cells. (B) Hydrodynamic diameter distribution of Blank-L, DDL and RDDL. (C) TEM images of DDL and RDDL, scale bar = 100 nm. (D) Changes in hydrodynamic diameter and PDI of RDDL for one week. (E) UV–vis absorption spectrum of DOX and DMF. (F) The release behaviors of DOX and DMF from RDDL in PBS (pH = 7.4). Data represented as Mean ± SEM (n = 3).

within 8 h, only 47% of DOX and 34% of DMF were released from RDDL under the same conditions. Such results demonstrated that RDDL effectively sustained drug release, facilitating near-synchronous delivery and synergistic therapeutic action *in vivo*.

3.3. CD20 expression on cells and cellular uptake

RTX, as the first therapeutic monoclonal antibody approved for cancer treatment, exhibits high specificity for the CD20 antigen [43,44]. Since the CD20 antigen is commonly expressed on B-cell malignancies, we performed several validation experiments to confirm its presence on SU-DHL-10 cells (GCB-like) [45]. Compared to tumor cells of non-B-cell origin, only SU-DHL-10 cells expressed the CD20 antigen (Fig. 3A), as confirmed by FCM results (Fig. 3B). Furthermore, we performed CLSM

to characterize using anti-CD20 antibodies (red fluorescence) and DAPI nuclear counterstain (blue fluorescence). The CLSM imaging revealed widespread distribution of CD20 across the cell membranes (Fig. 3C). These results successfully confirmed the presence of CD20 on SU-DHL-10 cells, which is consistent with existing knowledge [46]. Next, to evaluate the ability of RDDL to specifically recognize CD20, we co-incubated RDDL with SU-DHL-10, MCF-7, K562 and Jurkat cells for 1 h and 3 h, respectively. As shown in Fig. 3D–F, SU-DHL-10 cells exhibited the highest endocytosis of RDDL, which confirmed that RTX could enhance the ability of liposomes to recognize B cells.

Subsequently, we quantified cellular internalization over time using FCM and observed it through CLSM. We monitored the intracellular fluorescence intensity of DOX following incubation of the cells with DOX, DDL, and RDDL for 1, 2, 4, and 8 h. It can be observed that the
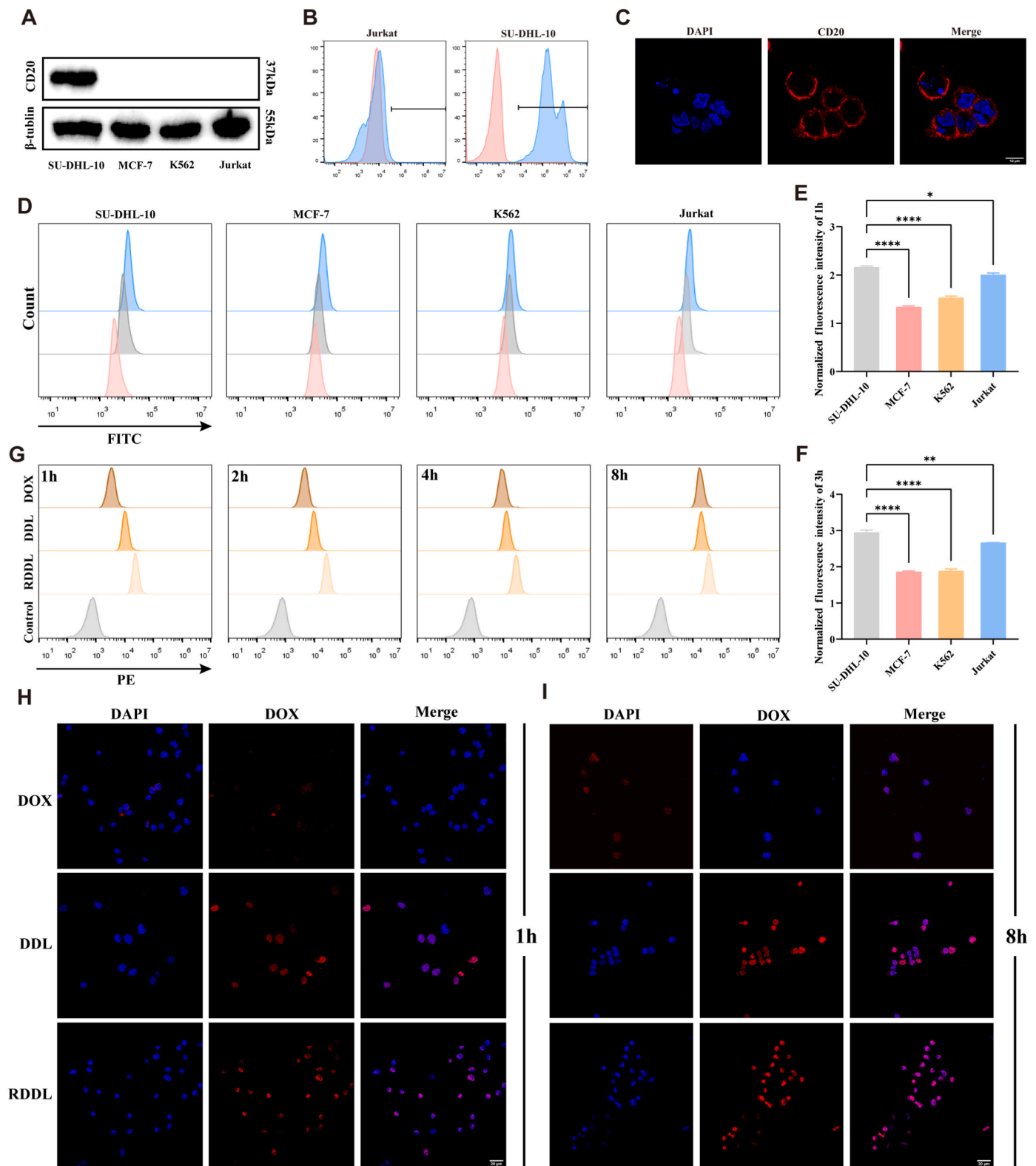
Fig. 3. CD20 expression on cells and cellular uptake. (A) CD20 protein expression of SU-DHL-10, MCF-7, K562 and Jurkat cells. (B) FCM analysis of CD20 in SU-DHL-10 and Jurkat cells. (C) CLSM images of SU-DHL-10 cells, scale bar = 10 μm. (D) Cellular uptake situations of SU-DHL-10, MCF-7, K562 and Jurkat cells after co-incubation with RDDL for 1 h (gary) and 3 h (blue). Normalized statistics of fluorescence intensity for (E) 1h and (F) 3h of cellular uptake. (G) FCM quantification of cellular uptake at 1, 2, 4, 8 h. CLSM images of SU-DHL-10 cells exposed to free DOX, DDL and RDDL for (H) 1 h and (I) 8 h, scale bar = 20 μm. Data represented as Mean ± SEM (n = 3). (For interpretation of the references to color in this figure legend, the reader is referred to the Web version of this article.)

fluorescence intensity exhibited a gradual increase over time, reaching its peak at 8 h (Fig. 3G). In CLSM images, we surprisingly found that DOX rapidly entered the cells and accumulated in the nucleus at 1 h. Notably, at both 1 and 8 h, the fluorescence intensity of DOX in RTX-modified liposomes was higher than that in unconjugated liposomes (Fig. 3H and I). These findings demonstrated that RTX significantly improved liposome targeting and enhanced cellular uptake.

3.4. RDDL induces apoptosis in SU-DHL-10 cells

Initially, we assessed the cytotoxicity of blank liposomes by co-culturing them with cells for 24 h. The results indicated that the blank liposomes were virtually non-toxic to the cells, suggesting an excellent safety profile for the nanocarrier (Fig. S8).

To compare the efficacy of free drugs and liposomes against SU-DHL-10 cells *in vitro*, we evaluated cell viability using the CCK-8 assay following treatment with PBS, DMF, DOX, DOX + DMF, DDL, and RDDL for 24 h, respectively. Results demonstrated that liposomes exhibited a more potent cytotoxic effect than free drugs, with RDDL showing greater efficacy than DDL (Fig. 4A). Additionally, Live/Dead staining assays were conducted, live cells emitted green fluorescence, while dead cells showed red fluorescence (Fig. 4B and C). Notably, the results were consistent with the CCK-8 assay outcomes. Annexin V/PI double staining was employed to evaluate the extent of apoptosis in cells, typically assessed by determining the ratio of early to late apoptotic cells. As shown in Fig. 4D and E, after a 24 h incubation with various formulations, the apoptosis rates for DDL and RDDL were significantly higher than those of the PBS and free drug groups. This suggested that the liposomes demonstrated superior cellular internalization and retention efficiency, leading to increased drug accumulation in the cytoplasm of SU-DHL-10 cells, resulting in a more potent killing effect.

To further elucidate the mechanism of action of the study drugs *in vitro*, we assayed ROS level, mitochondrial membrane potential (MMP), and apoptosis-related genes. Mitochondria play a pivotal role in the process of apoptosis. A decline in mitochondrial membrane potential heralds the early stage of apoptosis [47]. Therefore, JC-1 staining was utilized to evaluate the impact of the drugs on cellular MMP, results showed that DDL and RDDL significantly reduced the MMP by 53.42% and 66.1%, respectively (Fig. 4F and G). Since ROS serve as critical mediators of oxidative stress in tumor cells, the cellular ROS changes were also monitored using the 2,7-dichlorofluorescein diacetate (DCFH-DA) probe with FCM and CLSM. In CLSM imaging, the stronger green fluorescence indicates a higher level of ROS, and it can be visualized that the green fluorescence of RDDL is the strongest among all groups, which is consistent with the FCM results, proving RDDL maximally raised intracellular ROS levels, displaying the strongest anti-tumor effects (Fig. 4H-I and Fig. S9).

The p53-induced apoptosis pathway, associated with BH3 domain-containing proteins, is closely linked to the bcl-2 family of proteins [48]. The bcl-2 family proteins regulate the permeability of the mitochondrial outer membrane and other proteins, playing a pivotal role in the intrinsic mitochondrial apoptotic pathway [49]. Notably, the anti-apoptotic gene bcl-2 and the pro-apoptotic gene Bax are key regulators in mitochondria-mediated apoptosis [50,51]. Under normal conditions, Bax resides in the cytoplasm, but upon cellular stress, it translocates to the mitochondria, binds to bcl-2 family proteins, activates caspase 3, and ultimately induces apoptosis [52]. Firstly, the activation of intracellular caspase 3 was detected with a caspase 3 activity kit, and the experimental results showed that RDDL significantly elevated the activity of caspase 3 (Fig. 4J). To further confirm the intrinsic apoptotic pathway of RDDL, western blotting was used to examine the expression of apoptosis-related proteins in SU-DHL-10 cells. The results indicated that liposomes conjugated with RTX induced a decrease in bcl-2 and increased expression of p53, Bax, and caspase 3, suggesting that RDDL can indeed trigger apoptosis *via* the intrinsic pathway (Fig. 4K and L).

### 3.5. RDDL induce ferroptosis in SU-DHL-10 cells

Indeed, DMF has been shown to inhibit GCB-DLBCL cell lines (Fig. 4A). Some studies have revealed that DMF could induce ferroptosis in GCB-DLBCL cell lines *via* the System Xc⁻ pathway [32]. During aerobic cellular metabolism, GPX4 catalyzes the reduction of lipid hydroperoxides (LOOH) and GSH to their corresponding hydroxyl derivatives (LOH) and GSSG, respectively. When intracellular GSH level is inhibited by DMF, the catalytic activity of GPX4 was dose-dependently inhibited, leading to a marked decline in its capacity to detoxify LOOH, resulting in LPO (Fig. 5A).

Theoretically, RDDL can exert synergistic anti-tumor effects by enhancing ROS production through GSH depletion. Therefore, we investigated the changes in the intracellular GSH level. As displayed in Fig. 5B, compared with the control group, RDDL induced a significant decrease in intracellular GSH. Interestingly, DOX caused a substantial increase in GSH, likely representing a cellular adaptive response to oxidative stress—upregulating GSH to scavenge excess ROS. On the contrary, DMF directly reduced the level of GSH pools and reversed the high level of GSH induced by DOX. Meanwhile, the results in Fig. 4H and I showed that the combination of DMF and DOX enhanced the amount of ROS induced by DOX. The above results demonstrated that DMF can enhance the DOX-induced oxidative stress by reducing the intracellular GSH level, providing sufficient evidence that RDDL enhances apoptosis by depleting GSH.

To uncover the intrinsic mechanism behind RDDL's induction of ferroptosis in SU-DHL-10 cells, we further evaluated the impact of the drug treatments on the level of LPO and expression of GPX4 within the cells. As depicted in Fig. 5C, RDDL resulted in the highest MDA level. We subsequently detected the level of membrane LPO using the BODIPY581/591-C11 probe. Staining results showed that all treatment groups induced varying degrees of LPO, among them, RDDL displayed the strongest green fluorescence compared to controls, which indicated an increase in cellular LPO. Notably, DMF induced a certain degree of LPO, when combined with DOX, the level of LPO was further elevated. This is likely due to the involvement of the ROS-mediated pathway by DOX. As presented in the previous section, DOX can stimulate the production of ROS within cells (Fig. 4H and I). Accumulating research indicates that ROS play a crucial role in initiating and propagating LPO [53,54]. Thus, it is reasonable to expect that DOX promotes the DMF-mediated LPO generation through the ROS pathway, and FCM results confirmed these findings (Fig. 5D). Malondialdehyde (MDA), one of the products of LPO, was also measured. And western blotting results showed that RDDL could minimize the expression of GPX4 (Fig. 5E). The aforementioned results, in conjunction with Fig. 5B which revealed that, relative to the sole application of DMF, the DOX-DMF combination exerted a synergistic effect in reducing GSH levels, incontrovertibly confirmed that RDDL instigates the demise of SU-DHL-10 cells *via* DMF-mediated ferroptosis. Moreover, the DOX-mediated ROS signaling pathway served to further expedite this ferroptosis process.

Furthermore, when DDL and RDDL were co-treated with Fer-1 (a ferroptosis inhibitor), desferrioxamine (DFO, an iron chelator), the lipophilic antioxidant α-tocopherol (Vitamin E, VE), and GSH, we observed that GSH, Fer-1, and DFO effectively protected cells from RDDL-induced death (Fig. 5F and G). These results provided compelling evidence that RDDL induced ferroptosis. We hypothesized that a portion of the increase in cellular activity can be attributed to the fact that RDDL mainly exerts its anti-tumor effects through DOX-induced apoptosis, while DMF-induced ferroptosis plays a supporting role. Ultimately, these effects act synergistically to effectively induce cell death. Taken together, the aforementioned results confirmed that RDDL not only enhances the efficacy of apoptosis but also has the potential to induce ferroptosis, thereby exerting a dual apoptosis-ferroptosis therapeutic effect.
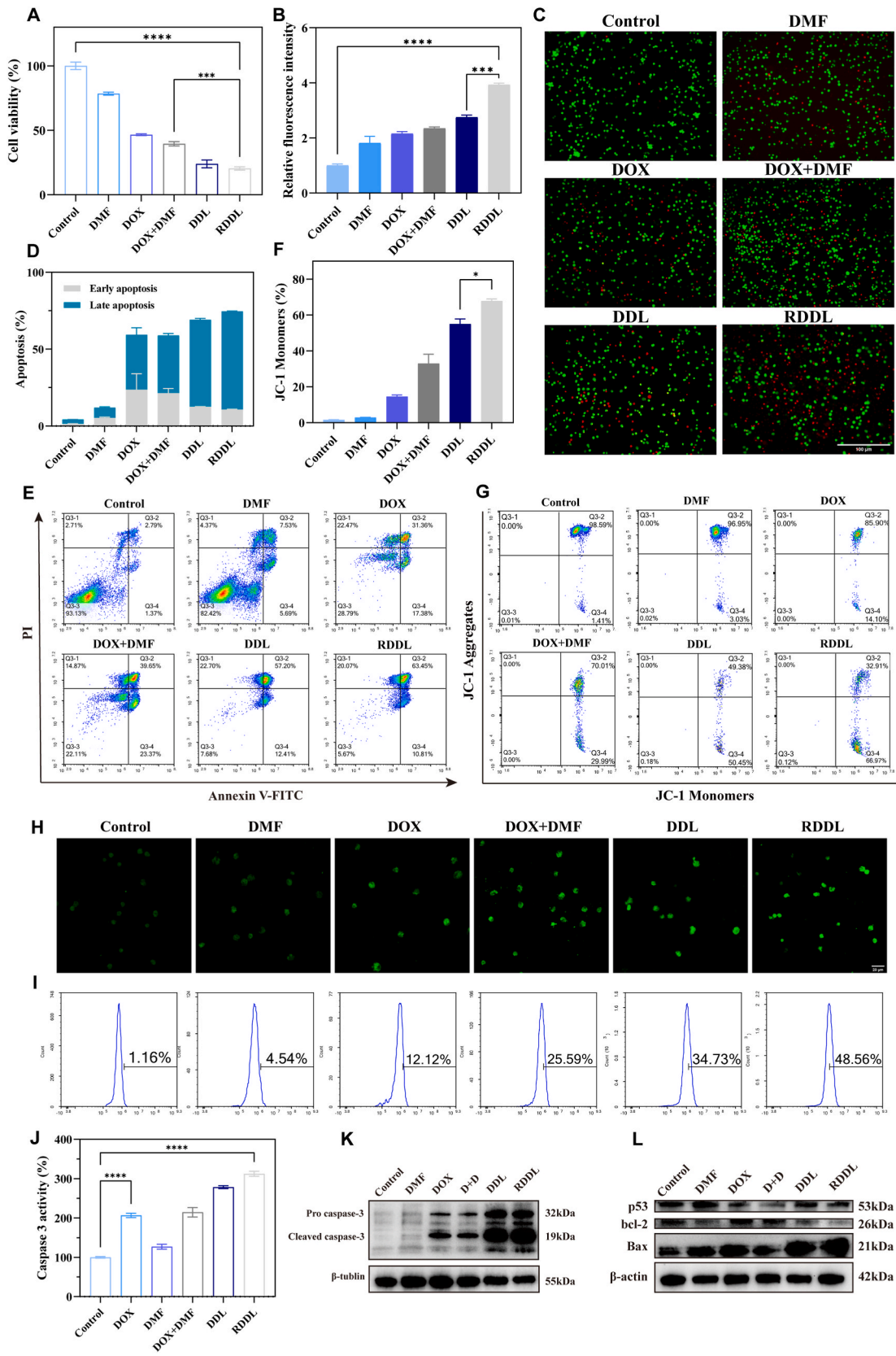
Fig. 4. RDDL inhibit SU-DHL-10 cells by inducing apoptosis. (A) Cell viability and (B) (C) Live/dead staining after treatment with PBS, DMF, DOX, DOX + DMF, DDL and RDDL for 24 h, scale bar = 100 μm. (E) Annexin V-FITC/PI apoptosis assay of SU-DHL-10 cells and (D) apoptosis ratio of treated cells. The changes of MMP in SU-HDL-10 cells after 24 h using (G) FCM and (F) quantification of the relative fluorescence intensity of JC-1 monomers. ROS level of SU-HDL-10 cells was detected by (H) CLSM and (I) FCM after 24 h. (J) Caspase 3 level of SU-HDL-10 cells after 24 h of treatment. Western blot of (K) pro caspase 3, cleaved caspase 3 and (L) p53, bcl-2, Bax expression in SU-HDL-10 cells after 24 h of various treatments. Data represented as Mean ± SEM (n = 3).
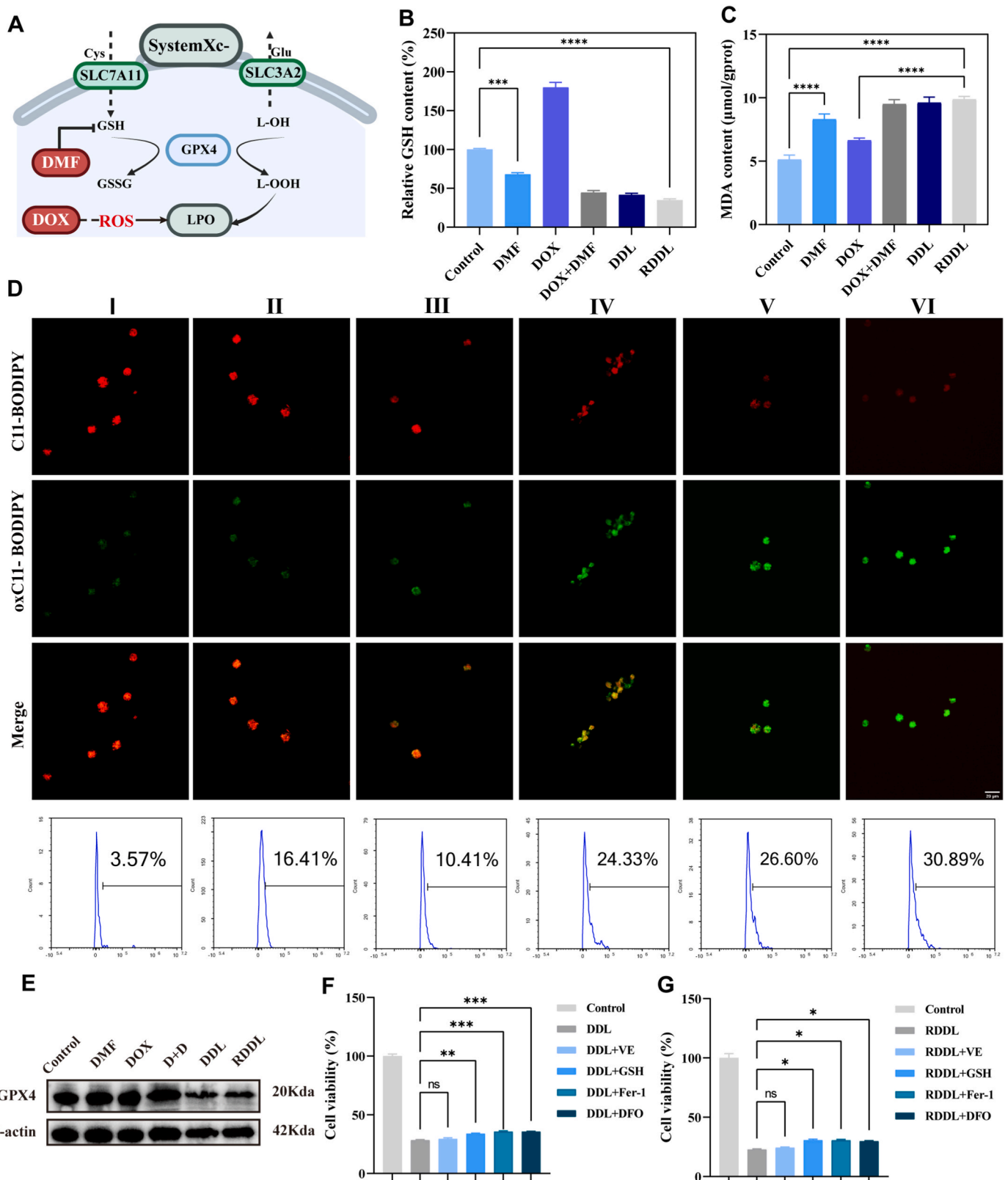
Fig. 5. RDDL inhibit SU-DHL-10 cells by inducing ferroptosis. (A) System X$_c^-$ signaling pathway, DMF leads to cellular LPO by directly reducing GSH. DOX accelerates lipid peroxidation by generating ROS. (B) Relative GSH content of SU-HDL-10 cells after 24 h of various treatments. (C) MDA content of SU-HDL-10 cells after 24 h of various treatments. (D) CLSM observation and FCM assay of LPO levels in SU-HDL-10 cells after 12 h of various treatments with BODIPY581/591-C11 probe, I: Control; II: DMF; III: DOX; IV: DOX + DMF; V: DDL; VI: RDDL, scale bar: 20 μm. (E) Western blot of GPX4 expression in SU-HDL-10 cells after 24 h of various treatments. SU-HDL-10 cells were treated with DDL (F) and (G) RDDL alone, or in combination with Fer-1, α-tocopherol, DFO, or GSH, survival was quantified by CCK-8 assay after 24 h. Data represented as Mean ± SEM (n = 3).

3.6. In vivo drug distribution

Our designed nanocarrier, intended as an effective drug delivery system for cancer treatment, should ideally achieve precise localization within tumor tissues. To track the distribution of liposomes into mice, we conducted an *in vivo* biodistribution study. We encapsulated DiD, a fluorescent probe, within the liposome to monitor its targeting process in real time. The fluorescence intensity of RTX-modified liposome was significantly higher in the tumor than that of the unmodified liposome group at all time intervals (3, 6, 9, 12, 24 h), with a peak observed at 12 h (Fig. 6A and B). In addition, the fluorescence intensities of major tissue organs and tumors in mice at 24 h were demonstrated (Fig. 6C and D). This result indicated that the modification of liposomes with RTX enhanced their targeting ability to tumors and led to higher accumulation levels compared to unmodified liposomes.

3.7. In vivo anti-tumor effect study

Prior to *in vivo* experimentation, we performed hemolysis experiments with blank liposomes to assess their biological safety. Notably, even at a relatively high liposome concentration of 6 mg/mL, the hemolysis rate was maintained below 5 %, indicating the excellent biocompatibility of the nanocarrier (Fig. 7B).

The biodistribution study confirmed that the liposomes could efficiently deliver drugs to tumor tissues. Building on this, we further evaluated their therapeutic effects. When the tumor reached 100 mm^3, the mice were randomly divided into Saline, DMF, DOX, DOX + DMF, DDL and RDDL groups. Different formulations were intravenously or intraperitoneal injected into mice every other day for three short treatment cycles, and tumor volume and body weight of the mice were recorded every two days (Fig. 7A). Throughout the treatment period, no statistically significant differences in body weight were detected (Fig. 7C). The results showed that the control group exhibited an unchecked growth trend throughout the study, while all treatment groups showed a reduction in this trend compared to the control. Notably, at the end of the treatment course, the tumor volume of the RDDL group was the smallest, indicating the highest anti-tumor potency (Fig. 7D–G). To further evaluate therapeutic efficacy, at day 21 of the treatment period, tumor tissues isolated from different groups were subjected to H&E staining and TUNEL analysis. The results were in high agreement with aforementioned findings. Specifically, the RDDL group demonstrated the lowest tumor weights ultimately (Fig. 7H). Moreover, the *in vivo* immunohistochemical results were generally consistent with the *in vitro* analyses (Fig. 8A).

3.8. In vivo toxicity detection

The potential toxicity of drugs is a critical concern throughout the entire treatment process. In particular, DOX has faced limitations in its clinical application owing to its adverse impacts, such as weight loss and cardiotoxicity [55,56]. To assess these effects, we closely monitored the body weight changes in mice throughout the treatment period. It was noted that the body weight of mice administered free DOX initially decreased, and then started to gradually increase after the 10th day. The body weight of mice in the liposome-treated groups remained relatively stable (Fig. 7C). This observation suggested that encapsulating DOX in liposomes may mitigate the weight loss associated with DOX treatment.

In the subsequent analysis of cardiac H&E-stained sections from the mice, the results revealed distinct pathological changes in the DOX-treated group (Fig. 8B). The cardiomyocytes exhibited disordered alignment, nuclear enlargement, partial myofiber lysis, and the presence of inflammatory cell infiltration, all of which indicate myocardial damage. In addition to the role of liposomes, it is worth mentioning that co-administration with DMF resulted in a milder disarray of cardiomyocytes and a reduction in vacuolation, marking a significant improvement over the DOX-only group. This aligns with prior research demonstrating DMF's capacity to mitigate DOX-induced cardiotoxicity. Furthermore, serum levels of CK-MB and LDH were considerably
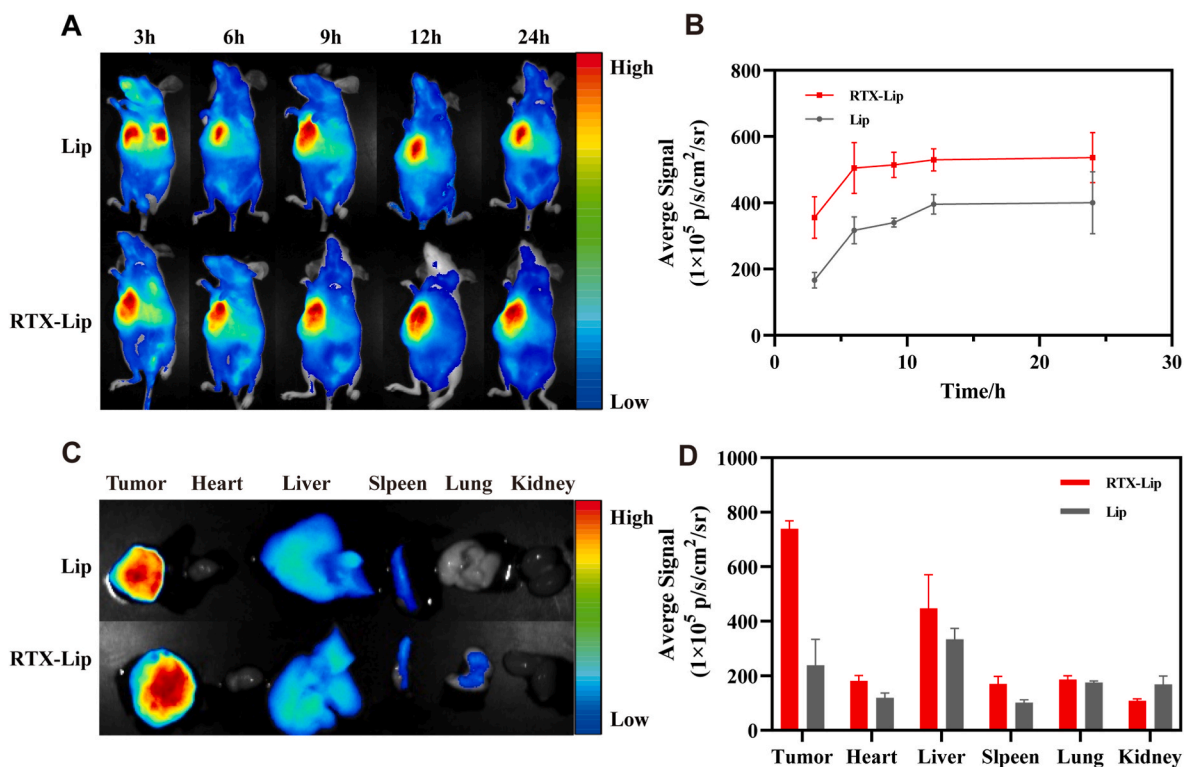

Fig. 6. *In vivo* drug distribution. (A) *In vivo* fluorescence imaging at 3, 6, 9, 12, 24 h after intravenous injection of liposome and RTX-Liposome. (B) Quantification of the mean fluorescence intensity in *in vivo* imaging. (C) Ex vivo imaging of the tumor and major organs at 24 h after liposome injection. (D) Quantification of the mean fluorescence intensity in ex vivo imaging. Data represented as Mean ± SEM (n = 3).
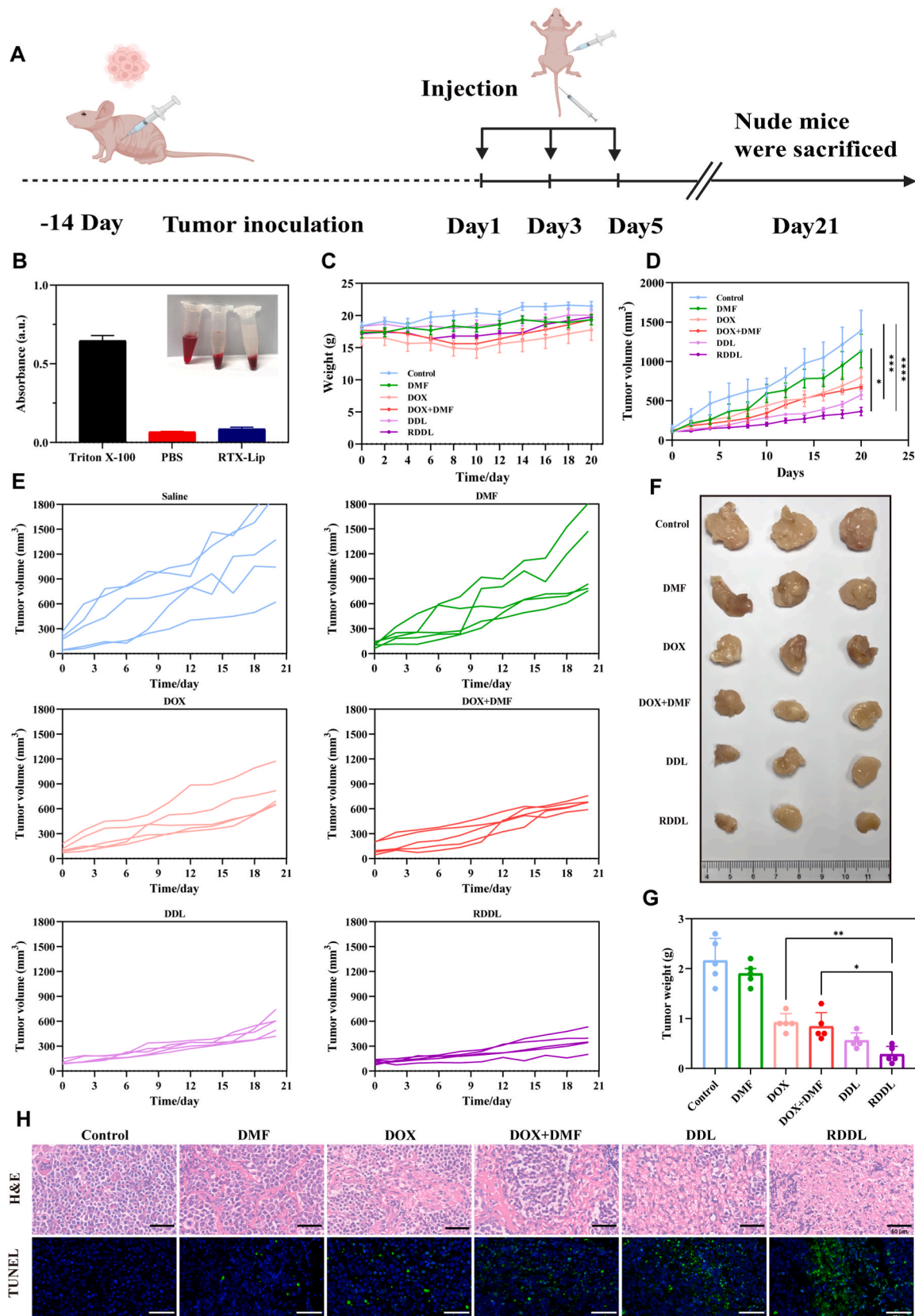
Fig. 7. *In vivo* anti-lymphoma effect study. (A) Schematic illustration of the dose regimen. Each group received an intravenous injection of various formulations with or without intraperitoneal injection of DMF. (B) Hemolysis assays of RTX-Liposome (n = 3). (C) Body weight of mice during treatment (n = 5). (D) The relative tumor growth curves of mice under different treatments (n = 5). (E) Individual tumor growth curves of SU-DHL-10 tumor-bearing mice with different treatments. (F) Representative photographs of the tumors harvested on day 21. (G) Tumor weight of mice after different treatments (n = 5). (G) H&E staining and TUNEL staining of tumor tissues after different treatments, scale bar = 50 μm. Data represented as Mean ± SEM.
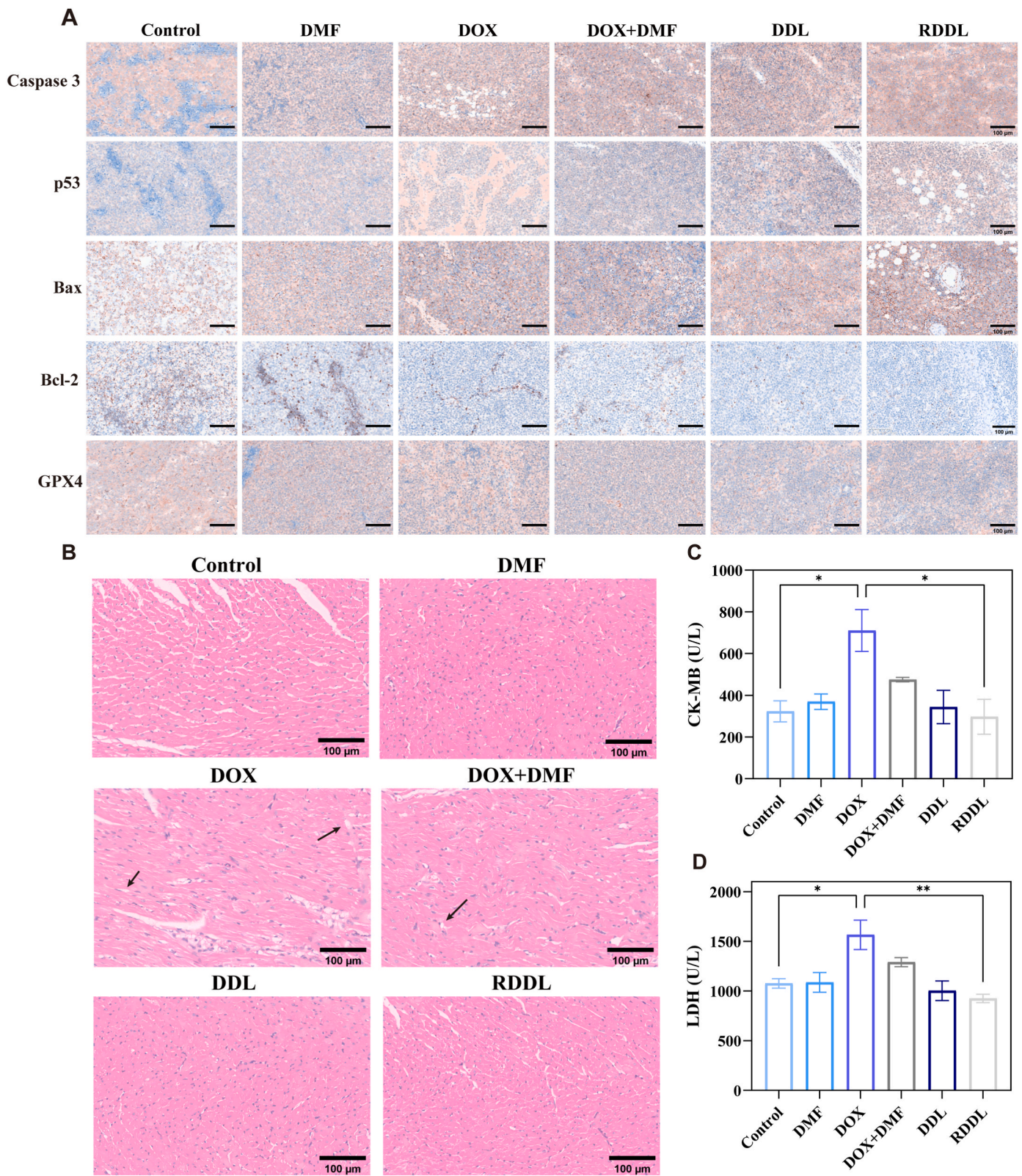
Fig. 8. *In vivo* immunohistochemistry and toxicity detection. (A) Caspase 3, p53, Bax, bcl-2, GPX4 immunohistochemical staining of tumor tissues after different treatments, scale bar = 100 μm. (B) H&E staining of heart after different treatments (the black arrows indicate myocardial injury, scale bar = 100 μm. Changes in serum levels of (C) CK-MB and (D) LDH (n = 5). Data represented as Mean ± SEM.

elevated in the DOX group when compared to the control group ([Fig. 8](#)C and D). Other major organs (liver, spleen, lungs and kidneys) were examined by H&E staining to assess the toxicity of the various treatments. There were no significant morphological differences in the tissue sections obtained from the treated group compared to the control group ([Fig. S10](#)). Serum biochemistry data indicated that DOX induced minor hepatic injury, whereas DDL and RDDL did not exhibit any significant deviation from the control group. These findings underscored the exceptional biocompatibility of the formulated liposomes ([Fig. S11](#)).

4. Conclusion

Herein, we successfully prepared CD20-targeted liposomes co-encapsulating DOX and DMF with excellent dispersion and stability. The nanomedicine enhanced the targeting of SU-DHL-10 cells, which allowed the two drugs to be delivered to the tumor site simultaneously and precisely, demonstrating a good anti-GCB-DLBCL efficacy.

Our preliminary findings highlight the synergistic anti-tumor effects of DOX and DMF. The anti-tumor mechanism of RDDL is characterized by a two-pronged regulation: DOX induces cell death by activating the ROS-mediated mitochondrial apoptotic pathway, whereas DMF depletes intracellular GSH through inhibition of the System Xc⁻, which in turn triggers ferroptosis in GCB-DLBCL cells. Notably, the depletion of GSH can lead to the persistent accumulation of ROS. This dynamic imbalance not only enhances apoptosis by disrupting the redox homeostasis but also further amplifies the ferroptosis effect. This bidirectional positive feedback mechanism has been validated in both *in vitro* and *in vivo* experiments. Importantly, RDDL not only exerted powerful anti-tumor effects, but also demonstrated significant cardioprotective functions. By constructing RTX-targeted co-loaded DOX/DMF liposomes (RDDL), the present study proposed for the first time a three-in-one therapeutic strategy of "chemo-sensitization-programmed death synergy-cardioprotection" (apoptosis-ferroptosis), which provides a new theory for overcoming the drug resistance of GCB-DLBCL, and also provides a new direction for other tumors.

CRediT authorship contribution statement

Shu-xian Liu: Writing – original draft, Investigation, Data curation. **Jun-yu Zhang:** Software, Formal analysis. **Xiao-yan Zheng:** Methodology, Funding acquisition. **Yong-zhong Du:** Supervision, Conceptualization. **Xiang-min Tong:** Writing – review & editing, Funding acquisition.

Ethics approval and consent to participate

Experiments involving animals were approved for implementation by the Ethics Committee of the Laboratory Animal Center of Zhejiang University. Ethics Approval No.ZJU20240826.

Declaration of competing interest

The authors declare that they have no known competing financial interests or personal relationships that could have appeared to influence the work reported in this paper.

Appendix A. Supplementary data

Supplementary data to this article can be found online at https://doi.org/10.1016/j.mtbio.2025.101844.

Abbreviations

FT-IR	Fourier-transform infrared
NMR	Nuclear magnetic resonance
DLBCL:	Diffuse large B-cell lymphoma
DOX	Doxorubicin
DMF	Dimethyl fumarate
RTX	Rituximab
GSH	Glutathione
NHL:	Non-Hodgkin's lymphoma
IHC	Immunohistochemical
GCB	Germinal center B cell
ABC	Activated B cell
GSSG	Generate oxidized glutathione
PDI	Polydispersity index
TEM	Transmission electron microscopy
DLS	Dynamic light scattering
FCM	Flow cytometry
CLSM	Confocal laser scanning microscopy
MMP	Mitochondrial membrane potential
System X_c^-:	Cystine-glutamate antiporter
LOOH	Lipid hydroperoxide derivatives
LOH	Hydroxyl derivatives
GPX4	Glutathione peroxidase 4
LPO	Lipid peroxidation
MDA	Malondialdehyde
DFO	Deferoxamine
VE	Lipophilic antioxidant alpha-tocopherol

Data availability

Data will be made available on request.

References

[1] K.C. Thandra, A. Barsouk, K. Saginala, S.A. Padala, A. Barsouk, P. Rawla, Epidemiology of non-hodgkin's lymphoma, Med Sci Basel Switz 9 (2021) 5.

[2] S.S. Wang, Epidemiology and etiology of diffuse large B-cell lymphoma, Semin. Hematol. 60 (2023) 255–266.

[3] R. Singh, S. Shaik, B.S. Negi, J.P. Rajguru, P.B. Patil, A.S. Parihar, et al., Non-Hodgkin's lymphoma: a review, J. Fam. Med. Prim. Care 9 (2020) 1834–1840.

[4] R. Alaggio, C. Amador, I. Anagnostopoulos, A.D. Attygalle, IB. de O. Araujo, E. Berti, et al., The 5th edition of the World Health Organization classification of haematolymphoid tumours: lymphoid neoplasms, Leukemia 36 (2022) 1720–1748.

[5] A. Dobashi, Molecular pathogenesis of diffuse large B-cell lymphoma, J Clin Exp Hematop JCEH 56 (2016) 71–78.

[6] T. Urata, Y. Naoi, A. Jiang, M. Boyle, K. Sunami, T. Imai, et al., Distribution and clinical impact of molecular subtypes with dark zone signature of DLBCL in a Japanese real-world study, Blood Adv. 7 (2023) 7459–7470.

[7] G.S. Nowakowski, M.S. Czuczman, ABC, GCB, and double-hit diffuse large B-cell lymphoma: does subtype make a difference in therapy selection? Am Soc Clin Oncol Educ Book Am Soc Clin Oncol Annu Meet (2015) e449–e457.

[8] J. Zhang, Y. Gu, B. Chen, Drug-resistance mechanism and new targeted drugs and treatments of relapse and refractory DLBCL, Cancer Manag. Res. 15 (2023) 245–255.

[9] A. Major, S.M. Smith, DA-R-EPOCH vs R-CHOP in DLBCL: how do we choose? Clin Adv Hematol Oncol HO 19 (2021) 698–709.

[10] H. Imran, Y. Tang, S. Wang, X. Yan, C. Liu, L. Guo, et al., Optimized DOX drug deliveries via chitosan-mediated nanoparticles and stimuli responses in cancer chemotherapy: a review, Mol Basel Switz 29 (2023) 31.

[11] J. Ning, B. Ma, J. Huang, L. Han, Y. Shao, F. Wang, Integrated network pharmacology and metabolomics reveal the action mechanisms of vincristine combined with celastrol against colon cancer, J. Pharm. Biomed. Anal. 239 (2024) 115883.

[12] L. Mazur, A. Augustynek, A. Deptała, H.D. Halicka, E. Bedner, Effects of WR-2721 and cyclophosphamide on the cell cycle phase specificity of apoptosis in mouse bone marrow, Anti Cancer Drugs 13 (2002) 751–758.

[13] O. Morana, W. Wood, C.D. Gregory, The apoptosis paradox in cancer, Int. J. Mol. Sci. 23 (2022) 1328.

[14] X. Xu, Y. Lai, Z.-C. Hua, Apoptosis and apoptotic body: disease message and therapeutic target potentials, Biosci. Rep. 39 (2019) BSR20180992.

[15] M. Kciuk, A. Gielecińska, S. Mujwar, D. Kołat, Ż. Kałuzińska-Kołat, I. Celik, et al., Doxorubicin-an agent with multiple mechanisms of anticancer activity, Cells 12 (2023) 659.

[16] S.B. Howerton, A. Nagpal, L.D. Williams, Surprising roles of electrostatic interactions in DNA-ligand complexes, Biopolymers 69 (2003) 87–99.

[17] R.N. Montalvo, V. Doerr, K. Min, H.H. Szeto, A.J. Smuder, Doxorubicin-induced oxidative stress differentially regulates proteolytic signaling in cardiac and skeletal muscle, Am. J. Physiol. Regul. Integr. Comp. Physiol. 318 (2020) R227–R233.

[18] Z. Liang, Y. Chen, R. Gu, Q. Guo, X. Nie, Asiaticoside prevents oxidative stress and apoptosis in endothelial cells by activating ROS-dependent p53/bcl-2/caspase-3 signaling pathway, Curr. Mol. Med. 23 (2023) 1116–1129.

[19] S.J.F. Chong, I.C.C. Low, S. Pervaiz, Mitochondrial ROS and involvement of Bcl-2 as a mitochondrial ROS regulator, Mitochondrion 19 (Pt A) (2014) 39–48.

[20] J. Jh, P. Cy, S. Eg, S. Ih, K. Jy, J. C, et al., Lactucin induces apoptosis through reactive oxygen species-mediated BCL-2 and CFLARL downregulation in Caki-1 cells, Genes Genomics 43 (2021).

[21] M. Dong, Y. Ding, J. Liu, Z. Xu, H. Hong, H. Sun, et al., Molecular insights of 2,6-dichlorobenzoquinone-induced cytotoxicity in zebrafish embryo: activation of ROS-mediated cell cycle arrest and apoptosis, Environ. Toxicol. 38 (2023) 694–700.

[22] M. Swamydas, E.V. Murphy, J.J. Ignatz-Hoover, E. Malek, J.J. Driscoll, Deciphering mechanisms of immune escape to inform immunotherapeutic strategies in multiple myeloma, J Hematol OncolJ Hematol Oncol 15 (2022) 17.

[23] C.M. Worsley, R.B. Veale, E.S. Mayne, The acidic tumour microenvironment: manipulating the immune response to elicit escape, Hum. Immunol. 83 (2022) 399–408.

[24] B. Niu, K. Liao, Y. Zhou, T. Wen, G. Quan, X. Pan, et al., Application of glutathione depletion in cancer therapy: enhanced ROS-based therapy, ferroptosis, and chemotherapy, Biomaterials 277 (2021) 121110.

[25] D.A. Averill-Bates, The antioxidant glutathione, Vitam Horm 121 (2023) 109–141.

[26] W. Zhong, F. Guo, F. Chen, M.-K. Law, J. Lu, D. Shao, et al., A multifunctional oxidative stress nanoamplifier with ROS amplification and GSH exhaustion for enhanced chemodynamic therapy, Front. Pharmacol. 13 (2022) 1044083.

[27] X. Chen, R. Kang, G. Kroemer, D. Tang, Broadening horizons: the role of ferroptosis in cancer, Nat. Rev. Clin. Oncol. 18 (2021) 280–296.

[28] H. Chen, C. Wang, Z. Liu, X. He, W. Tang, L. He, et al., Ferroptosis and its multifaceted role in cancer: mechanisms and therapeutic approach, Antioxid Basel Switz 11 (2022) 1504, https://doi.org/10.3390/antiox11081504.

[29] J. Liu, R. Kang, D. Tang, Signaling pathways and defense mechanisms of ferroptosis, FEBS J. 289 (2022) 7038–7050.

[30] X. Jiang, B.R. Stockwell, M. Conrad, Ferroptosis: mechanisms, biology and role in disease, Nat. Rev. Mol. Cell Biol. 22 (2021) 266–282.

[31] H.A. Blair, Dimethyl fumarate: a review in relapsing-remitting MS, Drugs 79 (2019) 1965–1976.

[32] A. Schmitt, W. Xu, P. Bucher, M. Grimm, M. Konantz, H. Horn, et al., Dimethyl fumarate induces ferroptosis and impairs NF-κB/STAT3 signaling in DLBCL, Blood 138 (2021) 871–884.

[33] U.G. Knaus, Oxidants in physiological processes, Handb. Exp. Pharmacol. 264 (2021) 27–47.

[34] D. Averill-Bates, Reactive oxygen species and cell signaling. Review, Biochim. Biophys. Acta Mol. Cell Res. 1871 (2024) 119573.

[35] H. Zheng, N. Xu, Z. Zhang, F. Wang, J. Xiao, X. Ji, Setanaxib (GKT137831) ameliorates doxorubicin-induced cardiotoxicity by inhibiting the NOX1/NOX4/reactive oxygen species/MAPK pathway, Front. Pharmacol. 13 (2022) 823975.

[36] Z. Zhong, Y. Tian, X. Luo, J. Zou, L. Wu, J. Tian, Extracellular vesicles derived from human umbilical cord mesenchymal stem cells protect against DOX-induced heart failure through the miR-100-5p/NOX4 pathway, Front. Bioeng. Biotechnol. 9 (2021) 703241.

[37] J. Gehl, M. Boesgaard, T. Paaske, B. Vittrup Jensen, P. Dombernowsky, Combined doxorubicin and paclitaxel in advanced breast cancer: effective and cardiotoxic, Ann Oncol Off J Eur Soc Med Oncol 7 (1996) 687–693.

[38] M. Sohail, Z. Sun, Y. Li, X. Gu, H. Xu, Research progress in strategies to improve the efficacy and safety of doxorubicin for cancer chemotherapy, Expert Rev. Anticancer Ther. 21 (2021) 1385–1398.

[39] X. Li, Doxorubicin-mediated cardiac dysfunction: revisiting molecular interactions, pharmacological compounds and (nano)theranostic platforms, Environ. Res. 234 (2023) 116504.

[40] R.G.R. Pinheiro, A. Granja, J.A. Loureiro, M.C. Pereira, M. Pinheiro, A.R. Neves, et al., RVG29-Functionalized lipid nanoparticles for quercetin brain delivery and Alzheimer's disease, Pharm. Res. 37 (2020) 139.

[41] Z. Yan, Y. Yang, X. Wei, J. Zhong, D. Wei, L. Liu, et al., Tumor-penetrating peptide mediation: an effective strategy for improving the transport of liposomes in tumor tissue, Mol. Pharm. 11 (2014) 218–225.

[42] Y. Chu, D. Li, Y.-F. Luo, X.-J. He, M.-Y. Jiang, Preparation and in vitro evaluation of glycyrrhetinic acid-modified curcumin-loaded nanostructured lipid carriers, Mol Basel Switz 19 (2014) 2445–2457.

[43] G. Salles, M. Barrett, R. Foà, J. Maurer, S. O'Brien, N. Valente, et al., Rituximab in B-cell hematologic malignancies: a review of 20 Years of clinical experience, Adv. Ther. 34 (2017) 2232–2273.

[44] R. L, C. N, S. M, K. C, C. Ti, T. C, et al., Structure of CD20 in complex with the therapeutic monoclonal antibody rituximab, Science 367 (2020).

[45] M.J.E. Marshall, R.J. Stopforth, M.S. Cragg, Therapeutic antibodies: what have we learnt from targeting CD20 and where are we going? Front. Immunol. 8 (2017) 1245.

[46] P. G, M. M, The regulation and function of CD20: an "enigma" of B-cell biology and targeted therapy, Haematologica 105 (2020).

[47] S. Bu, A. Xiong, Z. Yang, F. Chen, Y. Zhang, et al., Bilobalide induces apoptosis in 3T3-L1 mature adipocytes through ROS-mediated mitochondria pathway, Mol Basel Switz 28 (2023) 6410.

[48] J. Chen, The cell-cycle arrest and apoptotic functions of p53 in tumor initiation and progression, Cold Spring Harb. Perspect. Med. 6 (2016) a026104.

[49] W. Tan, Y. Li, L. Ma, X. Fu, Q. Long, F. Yan, et al., Exosomes of endothelial progenitor cells repair injured vascular endothelial cells through the Bcl2/Bax/Caspase-3 pathway, Sci. Rep. 14 (2024) 4465.

[50] L. Huang, J. Han, D. Ben-Hail, L. He, B. Li, Z. Chen, et al., A new fungal diterpene induces VDAC1-dependent apoptosis in Bax/Bak-deficient cells, J. Biol. Chem. 290 (2015) 23563–23578.

[51] J.A. Kim, J.C. Kim, J.S. Min, I. Kang, J. Oh, J.K. Ahn, HSV-1 ICP27 induces apoptosis by promoting Bax translocation to mitochondria through interacting with 14-3-3θ, BMB Rep. 50 (2017) 257–262.

[52] S. Li, H. Zhang, J. Zhang, Z. Zhang, X. Zhang, X. Zhang, et al., ALLN hinders HCT116 tumor growth through Bax-dependent apoptosis, Biochem. Biophys. Res. Commun. 437 (2013) 325–330.

[53] P. Luo, D. Liu, Q. Zhang, F. Yang, Y.-K. Wong, F. Xia, et al., Celastrol induces ferroptosis in activated HSCs to ameliorate hepatic fibrosis via targeting peroxiredoxins and HO-1, Acta Pharm. Sin. B 12 (2022) 2300–2314.

[54] X. Wang, T. Shen, J. Lian, K. Deng, C. Qu, E. Li, et al., Resveratrol reduces ROS-induced ferroptosis by activating SIRT3 and compensating the GSH/GPX4 pathway, Mol Med Camb Mass 29 (2023) 137.

[55] M. Songbo, H. Lang, C. Xinyong, X. Bin, Z. Ping, S. Liang, Oxidative stress injury in doxorubicin-induced cardiotoxicity, Toxicol. Lett. 307 (2019) 41–48.

[56] I.C. Jones, C.R. Dass, Doxorubicin-induced cardiotoxicity: causative factors and possible interventions, J. Pharm. Pharmacol. 74 (2022) 1677–1688.